A Characteristic Velocity for Gas-Fed PPT Performance Scaling *

J.K. Ziemer† and E.Y. Choueiri‡
Electric Propulsion and Plasma Dynamics Laboratory (EPPDyL)
MAE Department, Princeton University, Princeton, New Jersey 08544

This paper is dedicated to the memory of Dr. Daniel Birx

AIAA-2000-3432§

Abstract

The performance scaling of gas-fed pulsed plasma thrusters (GFPPTs) is investigated theoretically and experimentally. A characteristic velocity for GFPPTs that depends on the inductance-per-unit-length and the square root of the capacitance to initial inductance ratio has been identified. An analytical model of the discharge current predicts the efficiency to be proportional to the GFPPT performance scaling number, defined here as the ratio of the exhaust velocity to the GFPPT characteristic velocity. To test the validity of the predicted scaling relations, the performance of two rapid-pulse-rate GFPPT designs, PT5 (coaxial electrodes) and PT9 (parallel-plate electrodes), has been measured over 70 different operating conditions with argon propellant. The measurements demonstrate that the impulse bit scales linearly with the integral of the discharge current squared as expected for an electromagnetic accelerator. The measured performance scaling in both electrode geometries is shown to be in good agreement with theoretical predictions using the performance scaling number. Normalizing the exhaust velocity and the impulse-to-energy ratio by the GFPPT characteristic velocity collapses almost all the measured data onto single curves that represent the scaling relations for these GFPPTs.

*Research supported by the Air Force Office of Scientific Research, grant number: F49620-98-1-0119 and the Plasma Science and Technology Program at the Princeton Plasma Physics Lab.

†Graduate Student, Research Assistant. Member AIAA.

‡Chief Scientist at EPPDyL. Assistant Professor, Applied Physics Group. Senior Member AIAA.

§Presented at the 36^{th} AIAA Joint Propulsion Conference, Huntsville, AL, July 16-20, 2000.

1 Introduction

Gas-Fed Pulsed Plasma Thrusters (GFPPTs) are now being considered as a potential option for many station-keeping and primary propulsion missions. The benefits of GFPPTs include providing: specific impulse values as large as 10,000 s, arbitrarily low power requirements, easily throttled thrust output, small impulse bits for fine pointing, and the capability to use a large variety of propellant types. For these reasons, GFPPTs fill the requirements of many potential missions including NASA's Europa Orbiter, Pluto Fly-by and Space Interferometer missions [1], as well as DARPA's Orbital Express, and Motorola's Teledesic Constellation.

With the present focus on power-limited spacecraft, there is a need for an experimentally verified set of performance scaling relations for low energy GFPPTs. For the scaling laws to be useful, they should be simple and apply over a wide range of operating conditions and electrode configurations. They should also contain the main character of the acceleration physics while maintaining a good degree of accuracy so that they can be extended to low (or high) energy GFPPTs.

To accomplish this task, a number of previous attempts at deriving scaling laws were made (see Refs. [2] and [3] for example) and a number of performance studies on various thruster designs were conducted (see Refs. [4] and [5] for example). Yet, possibly because of the complex nature of the plasma acceleration in GFPPTs and the multitude of concurrent design changes at the time, the models did not accurately describe the exact performance scaling found in experimental measurements.

At Princeton's Electric Propulsion and Plasma Dynamics Lab (EPPDyL) a GFPPT has been designed in cooperation with Science Research Laboratory, Inc. (SRL) to explore performance scaling (see Refs. [6, 7, 8, 9, 10]). Using modern solid-state pulse forming technology to group series of low energy (<10 J) pulses together in bursts, the propellant mass utilization efficiency is maintained near 100% while eliminating the need for an ultra-fast valve with exceptional lifetime characteristics. The solid-state nature of the power conditioner also permits the system to be more compact and reliable than the previous single-pulse designs. In addition, the modular nature of the GFPPTs themselves has allowed testing of multiple iterations to examine the effects of changing various design parameters on performance. Simply stated, our goals concerning GFPPT performance scaling have been to:

- Derive universal scaling laws for GFPPT performance
- Experimentally verify the validity and extent of applicability of these laws
- Obtain physical insight into the basic mechanisms that impact the performance of GFPPTs
- Extend the understanding of how to build higher-performance devices and how to scale them to low (or high energies) while maintaining their high performance.

This paper describes the final results of the performance scaling studies, including both modeling and performance measurements of two GFPPT designs. First, the analytical model will be developed and the GFPPT characteristic velocity and the performance scaling number will be defined. Next, the performance measurements from two GFPPT designs with varying geometry, capacitance, energy, and mass bit will be presented. Finally, the measurements will be presented in terms of the GFPPT characteristic velocity and the performance scaling number to check the validity of the model.

2 Derivation of Performance Scaling Relations

As well known in PPT research, an effective circuit model can offer much insight into the discharge dynamics. Depending on the capacitance, C, initial inductance, L_0, inductance-per-unit-length, $L^{'}$, total resistance (including both the hardware and the effective plasma resistance), R, discharge energy, E, and the mass loading (shown schematically in 1), the discharge current has a damped oscillatory response with varying character: underdamped, critically damped, or overdamped. The circuit model is usually combined with a "snowplow" model for mass accumulation and numerically integrated to provide a solution that predicts performance at one operating condition. This technique has been used by these authors [7] and others [2, 3, 5, 11] to span possible operating conditions. Discovering analytical performance scaling relations from the numerical solutions of these non-linear differential equations, however, has proven difficult. Others have assumed a fixed inductance and a constant mass [12] or a slightly increasing mass from electrode erosion [13] to decouple the equations and provide analytical solutions. The scaling relations produced by these techniques, however, only apply to a very limited case of GFPPTs where the initial inductance and mass dominate the circuit response.

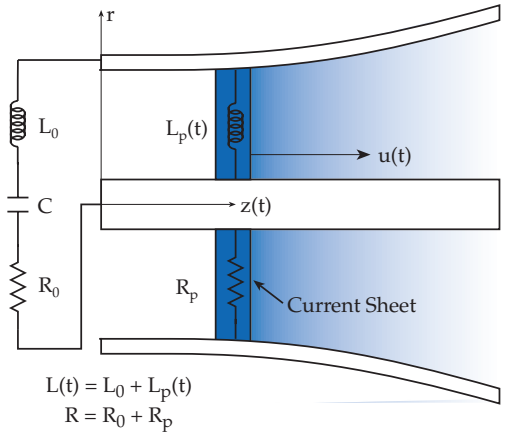

Figure 1: Schematic drawing of GFPPT discharge including elements used for the circuit model.

For the GFPPTs designed and tested by SRL and EPPDyL, the current waveform is essentially critically damped due to the low inductance (< 10 nH) and large capacitance (> 100μF) of the energy storage bank. Current waveforms measured with higher mass bits have a slight underdamped quality while lower mass bits can be slightly overdamped. With this understanding, we will focus on a "critical resis-

tance ratio,"

$$\psi \equiv \frac{R}{2}\sqrt{\frac{C}{L_0}}, \tag{1}$$

value near unity. As will be shown, this allows us to relax the assumptions of fixed inductance and mass used in Refs. [12, 13] and derive useful, analytical scaling relations for a more realistic model.

First, we expand Kirchhoff's equation for the effective discharge circuit,

$$V_0 = \frac{1}{C}\int_0^t J dt^* + (R + \dot{L})J + L\dot{J}, \tag{2}$$

where V_0 is the initial voltage on the capacitor and J is the total current flowing through the circuit. Solutions to this equation yield current waveforms, $J(t)$, with a character that depends on the changing inductance due to the motion of the current sheet. The total inductance at any given time is related to the position of the current sheet,

$$L = L^{'}z + L_0, \tag{3}$$

where z is the location of the current sheet down the length of the electrodes, and the value of $L^{'}$ depends on the electrode geometry. The momentum equation includes the self-induced Lorentz force in the axial direction,

$$\frac{d}{dt}(mu) = \frac{1}{2}\text{Ł}^{'}J^2, \tag{4}$$

where m is the instantaneous amount of mass contained in the current sheet moving at a velocity u.

Next, we split the discharge into two segments: before the peak current is reached at $t = t_{peak}$, and from that time until the current reaches zero, $t = t_{final}$. During each segment, we will assume that the current is *linearly* proportional to time. At the beginning of each segment, the values of $L(t), V(t), R$, and C will be used to determine the slope of the current waveform for the entire segment.

In the first segment, the slope of the current waveform is determined by the initial values of the inductance, L_0, and voltage, V_0, along with the fixed values of capacitance, C, and resistance, R. With these assumptions, the solution to Eqs. 2 and 4 has been given in Ref. [2] as,

$$J = \frac{V_0}{\omega L_0} e^{-(R/2L_0)t}\sin(\omega t), \tag{5}$$

where the natural frequency, ω,

$$\omega = \sqrt{\frac{1}{L_0 C} - \frac{R^2}{4L_0^2}} = \sqrt{\frac{1-\psi^2}{L_0 C}}. \tag{6}$$

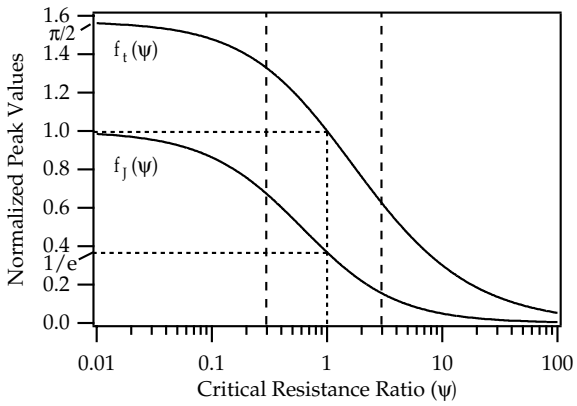

Figure 2: Normalized peak functions, $f_J(\psi)$ and $f_t(\psi)$, as a function of the critical resistance ratio, ψ. Values of the functions at $\psi = 1$ are shown by horizontal dashed lines. The range of ψ of interest to this study is $0.3 \leq \psi \leq 3$ as shown by the vertical dashed lines.

The peak current and the time at which it occurs can be found from this solution in terms of ψ,

$$J_{peak} = V_0\sqrt{\frac{C}{L_0}}\, f_J(\psi), \tag{7}$$

$$f_J(\psi) \equiv e^{-\left(\frac{\psi}{\sqrt{1-\psi^2}}\sin^{-1}(\sqrt{1-\psi^2})\right)}, \tag{8}$$

$$t_{peak} = \sqrt{L_0 C}\, f_t(\psi), \tag{9}$$

$$f_t(\psi) \equiv \left(\frac{1}{\sqrt{1-\psi^2}}\sin^{-1}(\sqrt{1-\psi^2})\right), \tag{10}$$

where $f_J(\psi)$ and $f_t(\psi)$ are designated as the "normalized peak functions". These two relations are shown as functions of ψ in Fig. 2 with exact values of the functions at $\psi = 1$ highlighted. The slope of the current in the first segment of the discharge is then simply J_{peak}/t_{peak},

$$J(t)|_0^{t_{peak}} = \frac{V_0}{L_0}\frac{f_J(\psi)}{f_t(\psi)}\, t. \tag{11}$$

In the next segment, our assumption of a close to critically damped waveform is very important in determining the correct slope of the current waveform approximation. For the critically damped case, the slope is related to the increasing inductance and exponentially decaying nature of the actual current

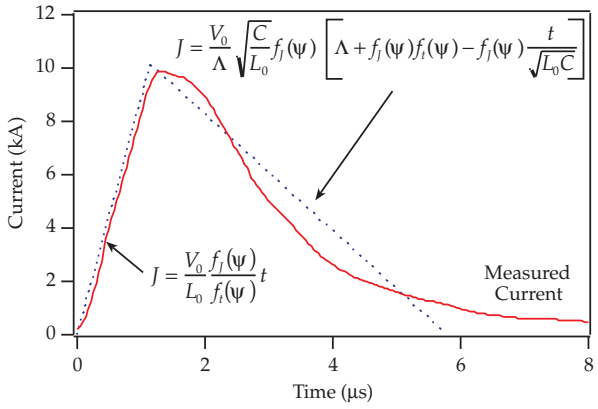

Figure 3: Variable element model for the current of a GFPPT discharge compared to a measured current trace from PT9: 4 J per pulse, 2.0 μg argon, 130 μF, 1" $\times$ 1" electrodes.

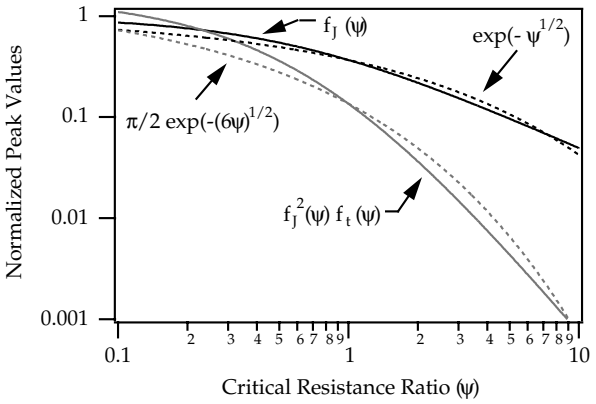

Figure 4: Approximations (dashed lines) to the normalized peak functions $f_J(\psi)$ and $f_J^2(\psi)$ (solid lines).

waveform. In this case, we will assume that the final slope is related to the total change in inductance, ΔL, by a factor Λ,

$$\Lambda \equiv \frac{L_f}{L_0} = 1 + \frac{\Delta L}{L_0}, \tag{12}$$

where L_f is the final inductance of the effective discharge circuit when the current sheet has reached the end of the electrodes, $L_f = L^{'}\ell_{electrodes}$. The second segment of the current waveform is then given by,

$$J(t)|_{t_{peak}}^{t_{final}} = \frac{V_0}{\Lambda}\sqrt{\frac{C}{L_0}}\, f_J(\psi) \times \left[\Lambda + f_J(\psi) f_t(\psi) - f_J(\psi)\frac{t}{\sqrt{L_0 C}}\right]. \tag{13}$$

The entire model for the current is shown with a measured current waveform from PT9 in Fig. 3 using the measured parameters of $L_0 = 10$ nH, $C = 130$ μF, and $V_0 = 242$ V. The approximate value of the inductance change, $\Lambda \approx 1.5$, is found by assuming that the current sheet reaches the end of the electrodes when the capacitor is fully drained. The model is shown to agree well with this current trace and the thruster parameters assuming $\psi \approx 1$.

As long as the effective resistance of the circuit does not change significantly during the discharge, i.e. ψ is constant, then the integral of J^2 can be evaluated in a straight-forward manner,

$$\int_0^{t_{final}} J^2 dt = \frac{2}{3} E \sqrt{\frac{C}{L_0}} \left[f_J^2(\psi) f_t(\psi) + f_J(\psi)\Lambda\right]. \tag{14}$$

Using Eqs. 8 and 10 to estimate the normalized peak functions for $0.3 \leq \psi \leq 3$,

$$\int_0^{t_{final}} J^2 dt = \frac{2}{3} E \sqrt{\frac{C}{L_0}} \left[\frac{\pi}{2} e^{-\sqrt{6\psi}} + \Lambda e^{-\sqrt{\psi}}\right]. \tag{15}$$

Theses approximations are shown in Fig. 4 to be in good order of magnitude agreement with the actual values of the normalized peak functions over the intended range of ψ, especially near $\psi = 1$. Now using this approximation to determine the impulse, we integrate the momentum equation (Eq. 4) to get the impulse bit, I_{bit},

$$I_{bit} = \int_0^{t_{final}} \left[\frac{d}{dt}(mu)\right] dt, \tag{16}$$

$$= \frac{1}{2} L^{'} \int_0^{t_{final}} J^2 dt, \tag{17}$$

$$= \frac{1}{3} E L^{'} \sqrt{\frac{C}{L_0}} \left[\frac{\pi}{2} e^{-\sqrt{6\psi}} + \Lambda e^{-\sqrt{\psi}}\right]. \tag{18}$$

Note that the *impulse* does not depend on how the propellant was accumulated. We have made no assumption of a constant mass in exchange for knowing only the exit conditions of the discharge. The trajectory of the current sheet during the discharge cannot be found without knowing the mass distribution. Although the mass distribution does not determine the impulse, it does determine the amount of *energy* required to accelerate the entire mass down the length of the electrodes to the exit velocity. This, in turn, effects the efficiency.

There is still one unknown in Eq. 18: Λ. To determine Λ, we add another constraint that the integral

of the current over the discharge time simply equal the initial charge on the capacitor, CV_0. This implies that the capacitor voltage at the end of the discharge is zero and that current no longer flows after t_{final}. Once again, we use Eqs. 11 and 13 to model the discharge current waveform and we find that,

$$\Lambda = 1 - f_t(\psi) f_J(\psi). \tag{19}$$

Using this relation, we can simplify the expression for the impulse bit,

$$I_{bit} = \frac{1}{3} E L' \sqrt{\frac{C}{L_0}}\, e^{-\sqrt{\psi}}. \tag{20}$$

Defining the exhaust velocity as,

$$u_e \equiv \frac{I_{bit}}{m_{bit}}, \tag{21}$$

The thruster efficiency, η_t, is then,

$$\begin{aligned} \eta_t &\equiv \frac{I_{bit}^2}{2 m_{bit} E}, && (22)\\ &= \frac{1}{6} L' \sqrt{\frac{C}{L_0}}\, u_e\, e^{-\sqrt{\psi}}, && (23)\\ &= \frac{u_e}{U}\, e^{-\sqrt{\psi}}, && (24)\\ &\propto \chi, && (25) \end{aligned}$$

where we have introduced the GFPPT characteristic velocity, U, as,

$$U \equiv \frac{6}{L'} \sqrt{\frac{L_0}{C}}, \tag{26}$$

and the GFPPT performance scaling number, χ, as

$$\chi \equiv \frac{u_e}{U}. \tag{27}$$

Note that if the total resistance in the circuit is zero ($\psi = 0$), then the maximum efficiency is reached when $u_e = U$ and $\chi = 1$. In this respect, the GFPPT characteristic velocity is the maximum obtainable exhaust velocity if there are no resistive losses in the complete discharge circuit. If $\psi > 0$, then the maximum exhaust velocity can be larger than U and χ can be greater than unity. The GFPPT characteristic velocity is only a function of the driving circuit and the electrode geometry making it *uniquely determined for each GFPPT design.*

The performance scaling number is a non-dimensional parameter that can be used to display performance measurements and check the validity of Eq. 25. Similarly, the non-dimensional impulse-to-energy ratio, $(I/E)^*$,

$$(I/E)^* = \frac{I_{bit}}{E} U, \tag{28}$$

is a useful non-dimensional parameter to compare thruster designs. Both the performance scaling number and the non-dimensional impulse-to-energy ratio will be used in the following section to examine performance scaling trends.

3 Measured Performance of GFPPTs

In order to determine if the performance scaling relations developed in the previous section are valid, two GFPPT designs were tested over a wide range of operational conditions. The two thrusters, PT5 and PT9, were developed specifically to observe the performance scaling trends using various mass bit, energy, capacitance, and inductance-per-unit-length values. PT5 was designed with a modular energy storage bank and coaxial electrodes to measure the effects of changing the capacitance and energy while keeping the inductance-per-unit-length constant. PT9 was designed with modular parallel-plate electrodes to measure the effects of changing the inductance-per-unit-length while keeping the capacitance and energy constant. Both designs were tested over an order of magnitude of argon propellant mass bit values.

The performance measurement techniques and the thrusters themselves have been described in Refs. [9, 10]. The performance of PT5 has been described in detail in Ref. [9] and a short summary will be provided in this section. The performance of PT9 with and without sidewalls will also be presented. Finally, the GFPPT characteristic velocity for each thruster design will be evaluated to normalize the performance data.

3.1 Performance of PT5

The coaxial electrode set of PT5 is shown in Fig. 5. PT5 was designed with a modular energy storage device using either a 130 or 270 μF capacitor bank to determine the effects of capacitance and energy on performance. As described in Ref. [9], PT5 showed two modes of operation depending on the mass bit. Figure 6 shows impulse bit measurements over a wide range of mass bit, capacitance, and energy levels. The

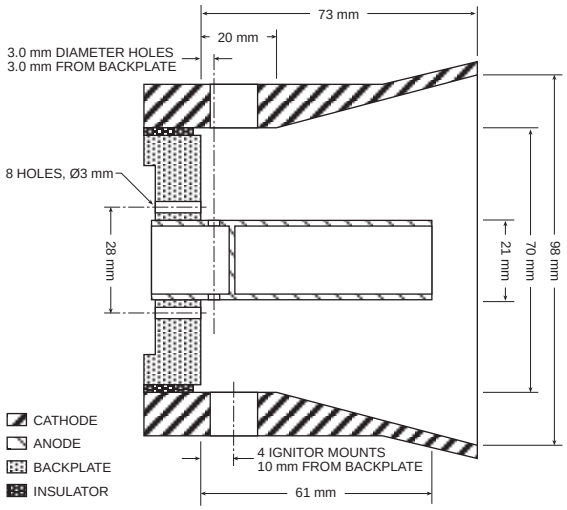

Figure 5: Schematic of PT5.

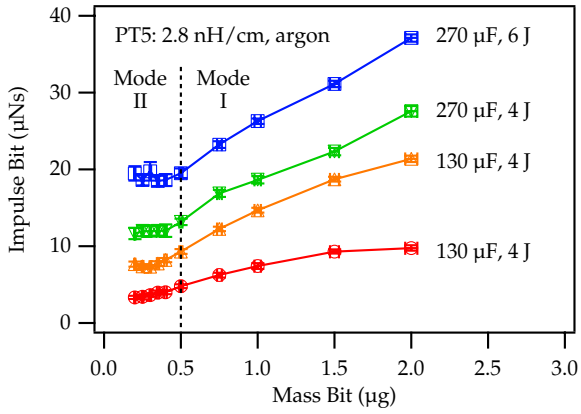

Figure 6: Measured impulse bit of PT5 with argon propellant at two capacitance and two energy values. Mode I and Mode II are also separated by the vertical dashed line and described in Section 3.1.

cut-off between Mode I and Mode II operation is near 0.5 μg per pulse and slightly decreases with decreasing capacitance. Mode I operation occurs for mass bit values above the cut-off and is characterized by an impulse bit and an impulse-to-energy ratio that increase with increasing mass bit. This leads to a relatively constant thruster efficiency in this mode of operation. In Mode II operation, the impulse bit and impulse-to-energy ratio are largely independent of the mass bit leading to an efficiency that varies linearly with exhaust velocity as expected by the model developed in the previous section. Possible explanations for Mode I operation are given in the appendix.

3.2 Performance of PT9

PT9 uses variable width (1" and 1/2") parallel-plates at two separation distances, (1" and 1/2") to vary the inductance-per-unit-length as shown in Fig. 7 and discussed in more detail in Ref. [10]. Three configurations were tested (a,b, and c) to measure the effect of increasing the inductance-per-unit-length while keeping the capacitance and energy constant near 130 μF and 4 J, respectively. The smallest value of inductance-per-unit-length (configuration a) was designed to be similar to the $L^{'}$ value of PT5.

3.2.1 Wall Losses in PT9

In Ref. [10] Pyrex sidewalls where used with PT9 to contain the propellant injected prior to the discharge. Figure 8 shows the change in the measured impulse bit from removing the sidewalls. These measurements suggest that two trends are competing depending on the mass bit and molecular weight of the propellant. It appears for both argon and helium that as the mass bit and pressure increase, the sidewalls may actually help to focus the exhaust stream. This is more the case for helium which has a larger thermal velocity for the same plenum temperature. In fact, since the pulse rate was kept constant in tests with both propellants, the propellant utilization efficiency may be much lower with helium, especially without sidewalls. In that case, a significant amount of helium may escape out of the electrode volume and not be accelerated by the discharge. With sidewalls, the performance with helium is better than the performance with argon by a slightly smaller factor than one would expect for a molecular phenomenon. In that case, the "drag" of ions hitting the sidewalls, recombining, and slowing to a thermal velocity determined by the surface temperature (much less than sheet speed) would be expected to scale with the *square root* of the atomic mass ratio, about 3.2. The discrepancy (the performance improvement was measured to be nearly a factor of 2.5) could be caused by the lower propellant utilization expected with helium.

Ion diffusion to the walls has been suspected before as a significant loss mechanism in magnetic shock tubes [14] and plasma guns [15]. In addition, if the current is carried at all by the ions in these discharges, then the cathode surface could also be retarding the bulk motion of the current sheet. Regardless of the

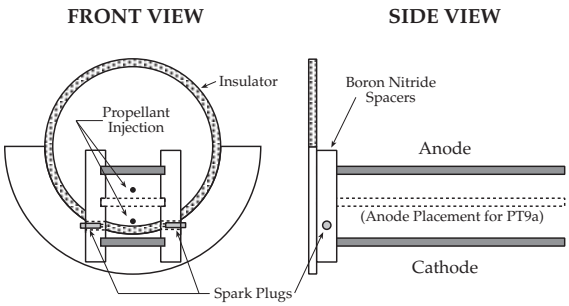

Figure 7: Schematic drawing of PT9b with 1" x 1" electrodes as well as the anode placement for PT9a. PT9c uses 1/2" wide electrodes with the same vertical 1" placement as PT9b.

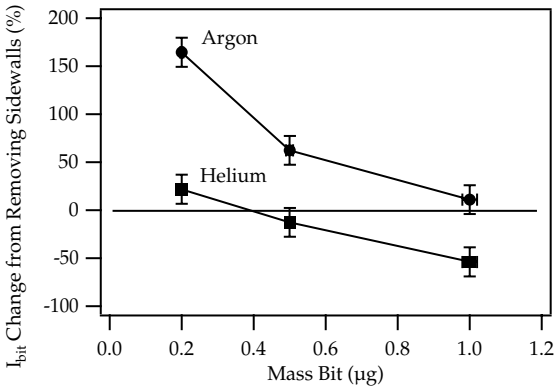

Figure 8: The percentage change in the measured impulse bit from removing pyrex sidewalls using both argon and helium propellants with PT9.

physical nature of the "drag", the negative effect of having any extra surface area exposed to the discharge is extremely apparent. For that reason, it was decided that the performance of PT9 was best measured again *without* sidewalls.

3.2.2 Performance of PT9 Without Sidewalls

The performance of PT9 over a wide range of mass bit values and three values of inductance-per-unit-length are shown in Fig. 9. In all these measurements, a 130 μF capacitor bank was used to keep the charging time requirements to a minimum with as little propellant escaping beyond the electrode volume as possible. The capacitors were charged up to approximately 250 V for each of six pulses in a burst. The maximum performance level measured with PT9 is with the highest inductance-per-unit-length configuration, 25% at 8,000 s I_{sp} with a 15 % efficiency measured near 5,000 s.

Note that there is no transition between two modes of operation expect, perhaps, near 0.5 μg per pulse in the lowest $L^{'}$ value of 2.8 nH/cm. In general, the efficiency varies linearly with the exhaust velocity as predicted by the model described in the previous section. The impulse-to-energy ratio increases close to linearly with increasing inductance-per-unit-length. Both of these trends will be discussed in more detail in the following section.

3.3 GFPPT Characteristic Velocity Values

The main design parameters for GFPPT hardware are the capacitance, initial inductance, and inductance-per-unit-length. These three parameters can be condensed into a single one that can effectively be used to predict performance: the GFPPT characteristic velocity, U, defined in Eq. 26. This characteristic parameter is derived from easily measurable quantities which are listed in Table 1 at the end of this paper. Note that larger values of U correspond to small capacitance and inductance-per-unit-length values.

4 Comparison of Scaling Relations with Measurements

Three scaling trends have been predicted by the model developed in Section 2:

1. The impulse bit should scale linearly with the integral of the current squared.
2. The impulse-to-energy ratio should be relatively constant over both mass bit and exhaust velocity.
3. The thruster efficiency should be linearly proportional to the non-dimensional exhaust velocity.

We will now examine these three predictions one at a time.

4.1 Impulse Bit Scaling with $\int J^2 dt$

Figure 10 shows the measured impulse bit as a function of the integral of $J^2(t)$ for both PT5 and PT9. With the open electrode design of PT9, deriving the current from the voltage waveform was difficult due

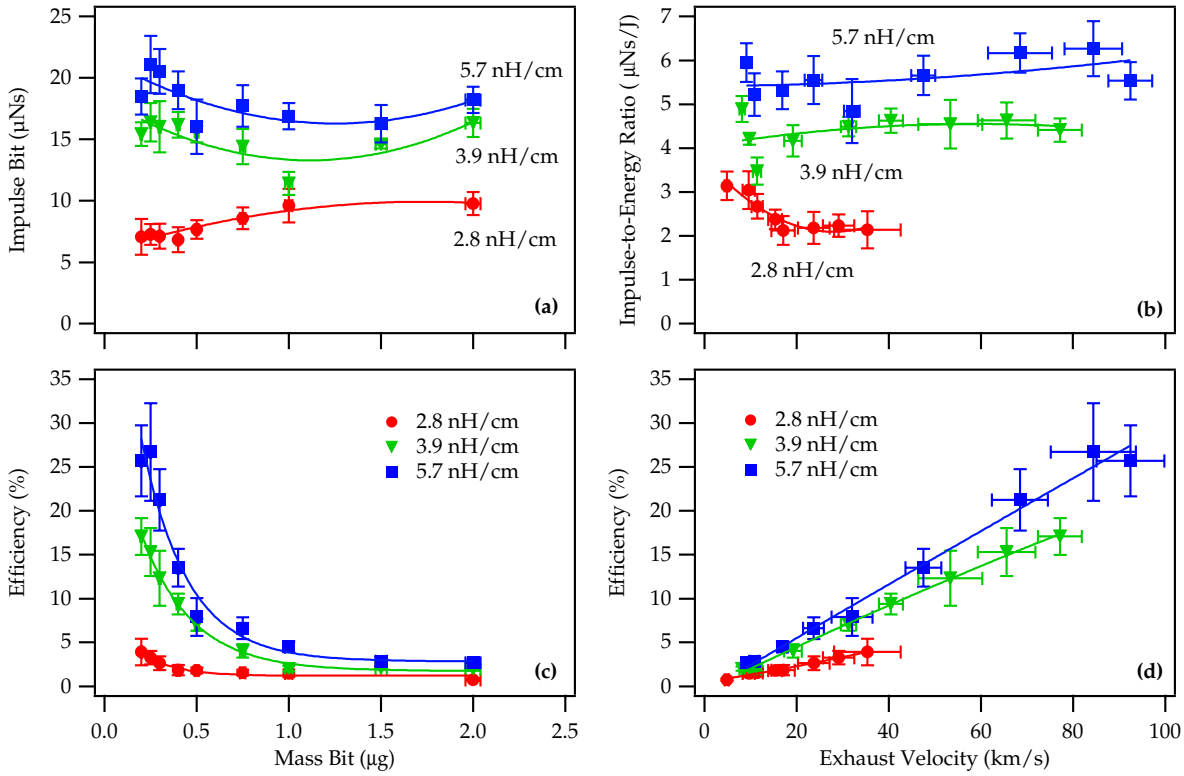

Figure 9: Measured performance of PT9 with argon, a 130 μF capacitor bank, approximately 4 J/pulse and the inductance-per-unit-length as a parameter. Graphs (a) and (c) show the impulse bit and thruster efficiency as a function of mass bit. Graphs (b) and (d) show the impulse-to-energy and thruster efficiency as a function of exhaust velocity.

Thruster		Geometry	Cap. (μF)	$L^{'}$ (nH/cm)	Energy (J)	U (km/s)
PT5	(a)	Coaxial	130	~ 2.8	2	190
	(b)	Coaxial	130	~ 2.8	4	190
	(c)	Coaxial	270	~ 2.8	4	130
	(d)	Coaxial	270	~ 2.8	6	130
PT9	(a)	P-Plate	130	2.8	4	190
	(b)	P-Plate	130	3.9	4	135
	(c)	P-Plate	130	5.7	4	92

Table 1: Thruster test configurations using argon propellant between 0.2-2.0 μg per pulse. Because PT5 has slightly flared electrodes the inductance-per-unit-length value, $L^{'}$, shown here is the average value. The inductance-per-unit-length values for PT9 are found using a conformal mapping technique of the electrode geometry as described in [10].

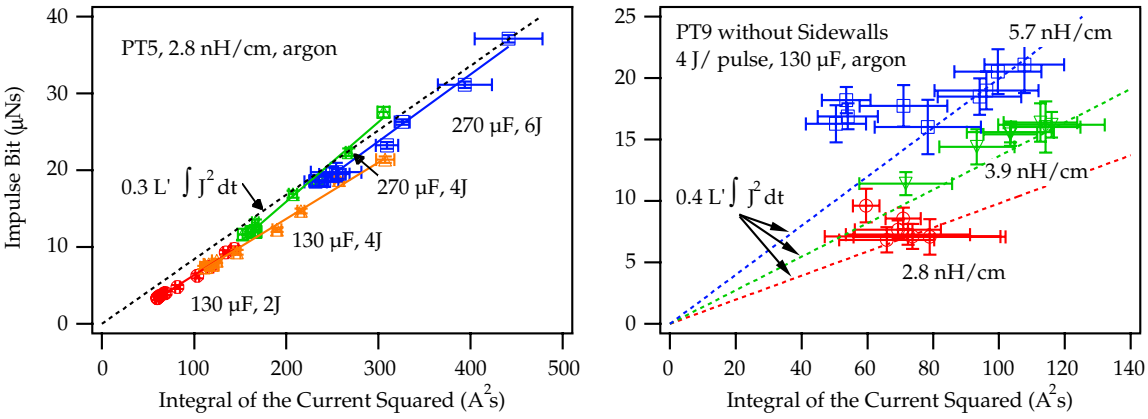

Figure 10: Impulse bit as a function of the integral of the current squared for both PT5 (left panel) and PT9 (right panel) over a wide range of operational conditions.

to EMI effects. Consequently, the errors are large for that measurement as reflected by the error bars in Fig. 10. Still, both thrusters show a linear trend as expected. Also note that for PT5 the integral of the current squared and the measured impulse bit both increase by as much as a factor of two for each curve. The integral of J^2 stays relatively fixed for PT9 although the impulse bit increases with increasing inductance-per-unit-length. For PT5, the inductance-per-unit-length does not change and the slope of a line going through the data in each case is very similar as expected.

From Eq. 17 the impulse bit should be proportional to $L^{'}/2 \int J^2 dt$. The slopes of the lines that agree with the measurements, however, are slightly smaller than predicted. This could be due to a number of loss mechanisms that are not accounted for by the model. These potential losses include energy going into unrecoverable plasma internal modes, profile losses from canted current sheets, and the conduction of ions to the cathode creating wall losses as described in Section 3.2.1. Again, although proportionally the impulse bit values are lower than expected, they do scale linearly with the integral of the current squared.

4.2 Impulse-to-Energy Ratio Scaling with Mass Bit

Graphs of the impulse-to-energy ratio as a function of mass bit for each thruster have already been shown in Fig. 6 and Fig. 9. Normalizing the impulse bit by the discharge energy and the GFPPT characteristic velocity, U, yields the non-dimensional impulse-to-energy ratio, $(I/E)^*$, as defined in Eq. 28. Using $(I/E)^*$ causes all the curves with varying capacitance, inductance-per-unit-length, and energy to collapse onto a single curve. In general, the trend of the impulse bit scaling with the energy level, the square root of the capacitance, and the inductance-per-unit-length is present throughout the data from both thrusters. At mass bit values below 0.5 μg, Both thrusters share a similar value of $(I/E)^*$ between 0.4 and 0.6, but PT5 has a larger value than PT9 at higher mass bits in Mode I operation. This trend will be examined in more detail in the appendix, however, for now it is important to notice that although there is an increase in $(I/E)^*$, it is similar for all four curves related to PT5.

For PT9, the three curves of $(I/E)^*$ are more similar at higher mass bits. The 1" x 1", 3.9 nH/cm configuration of PT9b seems to have the highest value at the lower mass bits. This could be due to it having slightly more propellant to accelerate compared to the 1/2" wide case of PT9c where more propellant might have escaped before the discharge was initiated. Compared to the 1/2" gap of PT9a, PT9b has a better electrode surface to volume ratio with a 1" gap, possibly reducing the amount of wall losses. Still, compared to the separated curves of the measured impulse bit in Fig. 9, the curves of $(I/E)^*$ in 11 are very similar.

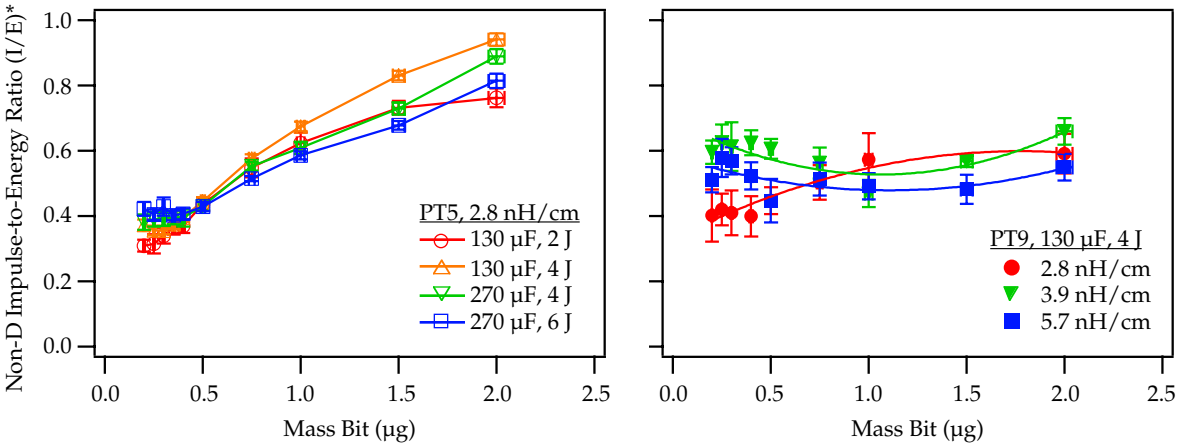

Figure 11: Impulse bit and non-dimensional impulse-to-energy ratio as a function of mass bit for both PT5 (left panel) and PT9 (right panel).

4.3 Efficiency Scaling with χ

Perhaps the most important prediction for the performance scaling of GFPPTs is that the efficiency is expected to scale linearly with the exhaust velocity. This trend was predicted by the model developed in Section 2, Eq. 24. Except for the Mode I operation (high mass bit, low exhaust velocity) in PT5, this is generally true from measured performance, as shown in Fig. 12. These graphs show the combined measurements for all seven configurations of the two GFPPT designs. In the left panel, the curves are spread out depending on capacitance, inductance-per-unit-length, and energy as the thruster efficiency is plotted versus the measured exhaust velocity. In the right panel, the thruster efficiency is plotted versus the performance scaling number, χ. Much of the data can be seen to collapse within 10% of a *single line*, $\eta_t = \chi/4$. This upholds the validity of the scaling model derived in Section 2 over a wide range of measured parameters. For the low-energy GFPPTs tested here, the efficiency is almost always related to the performance scaling number.

The linear coefficient of the line fit to the performance data, 1/4, corresponds to a critical resistance ratio of about 2 (see Eq. 25) which falls within the bounds of the model applicability. The largest deviations from this linear trend are at high mass bit values in PT5 Mode I operation and some slight deviations in PT9 at higher mass bit values. In the appendix we present four potential explanations for these deviations and argue that the plasma resistance could be decreasing at the higher mass bits. Smaller values of the effective plasma resistance reduce ψ and, hence, are likely to increase η_t.

5 Summary and Conclusions

An analytical model was used to derive performance scaling relations for GFPPTs. A central parameter to these relations is the GFPPT performance scaling number, defined as the ratio of the exhaust velocity to the GFPPT characteristic velocity. The relations were tested with an experimental data base over a range of 70 different operational conditions. The following conclusions can be drawn from this entire study:

- The thrust efficiency is directly proportional to the GFPPT performance scaling number for the conditions tested here,

$$\eta_t \propto \chi = \frac{u_e}{U} = \frac{1}{6} L' \sqrt{\frac{C}{L_0}}\, u_e. \qquad (29)$$

- For the low-energy GFPPTs studied here, the effective plasma resistance seems to be significant and plays an important role in determining performance.

- Wall losses were found to be important in the parallel-plate geometry and significantly higher

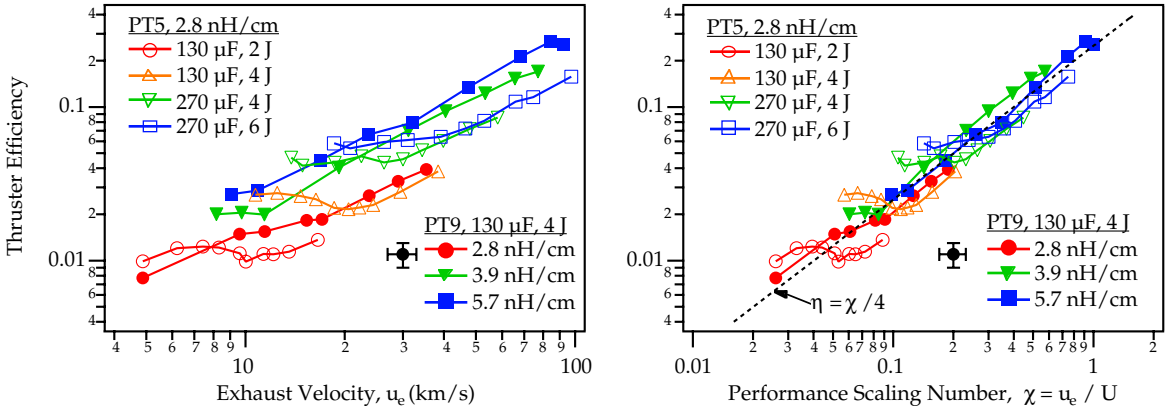

Figure 12: Thruster efficiency as a function of exhaust velocity and the performance scaling parameter, $\chi = u_e/U$, with a sample error bar shown near the legends. Using the performance scaling number allows almost all the data to fall close to one line, $\eta_t = \chi/4$.

performance has been measured without sidewalls.

- All measured performance data (η, u_e, and I_{bit}/E) can be made to collapse onto single, universal curves when non-dimensionalized according to the predicted scaling laws.

Although these scaling laws were tested over a wide range of parameters, it remains interesting to explore their validity at higher discharge energies and with different propellant types. Another remaining question is the explicit relation between the operating conditions and the plasma resistance which impacts the model through the parameter ψ. As research continues and with the use of the scaling relations derived here, GFPPTs have the potential to be useful for many spacecraft.

References

[1] J.J. Blandino and R.J. Cassady. Propulsion requirements and options for the new millennium interferometer (DS-3) mission. In 34^{th} *Joint Propulsion Conference*, Cleveland, OH, July 13-15 1998. AIAA 98-3331.

[2] R.G. Jahn. *Physics of Electric Propulsion*. McGraw-Hill, 1969.

[3] C.J. Michels, J.E. Heighway, and A.E. Johansen. Analytical and experimental performance of capacitor powered coaxial plasma guns. *AIAA Journal*, 4(5):823–830, May 1966.

[4] P. Gloersen, B. Gorowitz, and J.T. Kenney. Energy efficiency trends in a coaxial gun plasma engine system. *AIAA Journal*, 4(3):436–441, March 1966.

[5] P.J. Hart. Modified snowplow model for coaxial plasma acclerators. *Journal of Applied Physics*, 35(12):3425–3431, December 1964.

[6] J.K. Ziemer, E.A. Cubbin, E.Y. Choueiri, and D. Birx. Performance characterization of a high efficiency gas-fed pulsed plasma thruster. In 33^{rd} *Joint Propulsion Conference*, Seattle, Washington, July 6-9 1997. AIAA 97-2925.

[7] J.K. Ziemer and E.Y. Choueiri. Dimensionless performance model for gas-fed pulsed plasma thrusters. In 34^{th} *Joint Propulsion Conference*, Cleveland, Ohio, July 13-15 1998. AIAA 98-3661.

[8] J.K. Ziemer, T.E. Markusic, E.Y. Choueiri, and D. Birx. Effects of ignition on discharge symmetry in gas-fed pulsed plasma thrusters. In 34^{th} *Joint Propulsion Conference*, Cleveland, Ohio, July 13-15 1998. AIAA 98-3803.

[9] J.K. Ziemer, E.Y. Choueiri, and D. Birx. Is the gas-fed PPT an electromagnetic accelerator? an investigation using measured performance. In

35^{th} *Joint Propulsion Conference*, Los Angeles, California, June 20-24 1999. AIAA 99-2289.

[10] J.K. Ziemer, E.Y. Choueiri, and D. Birx. Comparing the performance of co-axial and parallel-plate gas-fed PPTs. In 26^{th} *International Electric Propulsion Conference*, Kitakyushu, JAPAN, October 17-21 1999. IEPC 99-209.

[11] M. Andrenucci, M. Caprili, and R. Lazzeretti. Theoretical performance of pulsed coaxial plasma guns. Technical report, Universita di Pisa, 1972.

[12] P.M. Mostov, J.L. Neuringer, and D.S. Rigney. Electromagnetic acceleration of a plasma slug. *The Physics of Fluids*, 4(9):1097–1104, September 1961.

[13] D.J. Vargo. Electromagnetic acceleration of a variable-mass plasma. Technical Report TN D-2164, NASA, 1964.

[14] J. Keck. Current speed in a magnetic annular shock tube. In *Proceedings of an International Symposium on Plasma Guns, Pysics of Fluids Supplement (Part II, Vol. 7(11))*, pages S16–S27, November 1964.

[15] k. Thom, J. Norwood, and N. Jalufka. Velocity limitation of a coaxial plasma gun. In *Proceedings of an International Symposium on Plasma Guns, Pysics of Fluids Supplement (Part II, Vol. 7(11))*, pages S67–S70, November 1964.

[16] W.J. Guman. Solid propellant pulsed plasma micro-thruster studies. In 6^{th} *Aerospace Sciences Meeting*, New York, New York, January 22-24 1968. AIAA 68-85.

[17] R.G. Jahn and W. von Jaskowsky. Current distributions in large-radius pinch discharges. *AIAA Journal*, 2(10):1749–1753, October 1964.

[18] R.B. Johansson. Current sheet tilt in a radial magnetic shock tube. *The Physics of Fluids*, 8(5):866–871, May 1965.

[19] L. Aronowitz and D.P. Duclos. Characteristics of the pinch discharge in a pulsed plasma accelerator. In E. Stuhlinger, editor, *Electric Propulsion Development*, volume 9 of *Progress in Astronautics and Rocketry*. Academic Press, 1963.

6 APPENDIX: Possible Explanations for Mode I

As seen in almost all the comparisons between measurements and models, the largest discrepancies occur for PT5 in Mode I operation. In this mode, the efficiency does not decrease monotonically with exhaust velocity and the impulse-to-energy ratio increases with increasing mass bit. So far, four different explanations for the higher than predicted performance have been proposed: electrothermal energy recovery, finite electrode length effects, increased profile or sweeping efficiency, or a decrease in the effective plasma resistance at higher mass bit values. The real explanation could be a combination of these ideas which we will now explore one at a time.

6.1 Electrothermal Energy Recovery

At the higher mass bit values of Mode I, the number density and pressure are higher and the mean free path is correspondingly lower compared to Mode II operation. If any electrothermal energy is to be recovered at all, it would be at Mode I conditions. The scaling relations suggested for a thruster where electrothermal acceleration is dominant, however, are quite different (see ref. [16] for example). In this case, the impulse bit is expected to scale with the *square root* of the discharge energy to mass bit ratio and not depend directly on capacitance or inductance change. This is a result of the energy deposited in the plasma being proportional to the integral of RJ^2. The *efficiency* of a pure electrothermal accelerator is expected to be constant over wide range of energy, exhaust velocity, and mass bit values. While the efficiency for PT5 is indeed independent of mass bit and exhaust velocity at high mass bit values (i.e. Mode I), it does show a dependence on energy.

Another contrary piece of information for this explanation is the relation between the impulse bit and integral of the current squared, as shown in Fig. 10. For an electrothermal thruster, the exhaust velocity and hence the impulse bit should scale as the square root of the integral of the current squared. Clearly this is not the case with the measured trends having more of a linear character as would be expected from an electromagnetic acceleration. In addition, even at mass bit values that clearly fall into Mode I operation, the impulse-to-energy ratio was found to be *constant* over a wide range of energy values as described in Ref. [9]. This is characteristic of an electromagnetic accelerator, not an electrothermal one. Therefore, al-

though some electrothermal energy may very well be recovered in these discharges, the amount is believed to be minor and not enough to explain Mode I operation.

6.2 Finite Electrode Length Effects

In Mode I operation, the discharge may not reach the end of the electrodes by the time the capacitor is fully drained. If there is a uniform propellant distribution before the pulse, then the current sheet would run into a large amount of unaccelerated propellant after the Lorentz force has stopped. This would impose a serious amount of drag on the sheet, however, the impulse bit would not be affected. With the amount of mass increasing at the same rate as the velocity is decreasing, the impulse bit is constant, however, the efficiency steadily *decreases*. Unfortunately this description is in opposition to the observed trend.

Instead, if there is an exponential propellant distribution, then the efficiency would be highest when the greatest amount of energy in the capacitor is transferred to the discharge. For the smaller mass bits, the current sheet may run to the end of the electrodes well before the capacitor is fully drained, reducing the efficiency. We would expect that as the velocity continues to increase and the electrode length is fixed, the efficiency would decrease as duration the current sheet is in contact with the electrodes decreases. Once again, this explanation does not match exactly with the observed performance trends.

6.3 Increased Sweeping and/or Profile Efficiency

Since these quantities have not been measured directly, it is difficult to determine if an increase in one or the other is indeed the cause for the higher than expected performance. In previous studies of current sheet structure in argon discharges, it has been noticed that the sweeping efficiency (the effectiveness of the current sheet to pick up propellant as it moves down the electrodes) increases with increasing current rise rates [2, 17]. An empirical rule of thumb is that 10^{12} A/s-cm over the span of the current sheet is required for 100% sweeping efficiency. Most of the low-energy GFPPT discharges presented here fall *just below* this 10^{12} A/s-cm cut-off. As seen in Fig. 10 the current does indeed increase as the mass bit value increases which could imply that the sweeping efficiency is improving. Still, as shown in Section 2, the *impulse* should not depend on how the mass was swept up. In other words, although the thrust efficiency should be sensitive to the sweeping efficiency, the impulse-to-energy ratio should not. In addition, both ref. [17] and ref. [18] showed that the sweeping efficiency *decreased* for higher mass bit values.

As far as the possibility of a profile efficiency increase in Mode I operation, once again the literature points towards the opposite of the trends we observe with mass bit and pressure. Using an inverse z-pinch device, Johansson found that the tilting of the current sheet (which causes profile losses) *increased* for higher mass bit values [18]. Although the profile efficiency should effect both the thruster efficiency and the impulse-to-energy ratio, the existing models appear to predict the opposite trend. In addition, the GFPPTs presented in this paper have much shorter electrodes compared to any accelerator where significant tilting and profile losses have been found to occur.

6.4 Decrease in Effective Plasma Resistance

Another possibility is based on the potentially changing value of ψ with the mass bit (which is related to the initial propellant density). As apparent in all the comparisons between predicted and measured performance, as the mass bit increases, the measured performance moves closer and closer to values that are predicted by smaller critical resistance ratios. As the initial inductance and capacitance are fixed, this would imply that the effective resistance in the circuit (capacitor internal impedance plus plasma resistance) is decreasing as the mass bit (and density) is increasing. Once again we turn to Fig. 10 to see that the current levels also increase at higher mass bit values. In fact, the mass bit cut-off between a relatively constant integral of J^2 and where the integral values begin to increase agrees well with the transition point found in Fig. 6. As expected, and found in previous experiments [14, 19], as both the energy and current increase, the effective plasma resistance drops. A decreasing value of ψ for the observed increasing performance of PT5 in Mode I operation is the most consistent explanation with all the observed trends presented here and in the literature.